

# INTERLAMINAR FRACTURE IN TUFTED COMPOSITES: EFFECTS OF TUFT GEOMETRY AND SURFACE DENSITY

Joncas, S.<sup>1\*</sup>, Pappas, G.<sup>2</sup>, Botsis, J.<sup>2</sup>, Michaud, V.<sup>3</sup>

<sup>1</sup> Automated Manufacturing Department, Ecole de Technologie Supérieure, Montréal, Canada

<sup>2</sup> Laboratory of Applied Mechanics and Reliability Analysis (LMAF), Ecole Polytechnique Fédérale de Lausanne, Lausanne, Suisse

<sup>3</sup> Laboratory for Processing of Advanced Composites (LPAC), Ecole Polytechnique Fédérale de Lausanne, Lausanne, Suisse

\* Corresponding author ( [simon.joncas@etsmtl.ca](mailto:simon.joncas@etsmtl.ca) )

**Keywords:** *Textile preform, Tufting, Fracture toughness*

## 1 ABSTRACT

This work investigated the effect of tuft geometry and tufting pattern on interlaminar fracture toughness (Mode I). First, using a 5mm square tufting pattern, the individual contribution of tufts and ply delamination to fracture resistance, conventionally described by the R-Curve, was investigated. This helped quantify the exact contribution of tufts to fracture resistance in tufted composites. Results showed that depending on tuft geometry (standard or with surface loops milled down), tufts can be responsible of up to 80% of the fracture resistance of tufted composites. Specimens with loops milled-down exhibited 60% more fracture resistance at steady state than specimens with standard tufting. This is attributed to the large amount energy required for tuft pull-out compared to tuft fracture during the delamination process. When compared to experimental results, numerical analysis on this 5mm square tufting pattern demonstrated that interlaminar fracture in tufted composites can be accurately predicted (within 10%) by superposing conventional bridging laws applied to cohesive elements and connector elements mimicking the tuft load/displacement response. Finally, to evaluate the effect of tufting patterns and density with respect to fracture resistance, a 4mm square pattern (6 tufts/cm<sup>2</sup>) and a 5mm staggered pattern (7.2 tufts/cm<sup>2</sup>) were compared to the 5mm square pattern (4 tufts/cm<sup>2</sup>). Results showed that increasing tufting areal density could significantly increase fracture resistance with some specimens reaching an ERR at steady state one order of magnitude higher than equivalent non-tufted specimens.

## 2 INTRODUCTION

Developments in automated assembly techniques for dry-fiber textiles now enable the production of complex through-the-thickness reinforced (TTR) preforms for various liquid molding composite material fabrication processes. Among the variety of assembly techniques, tufting was used successfully in different industrial applications for its simplicity and effectiveness as a TTR method (e.g. the Latecoere/Boeing 787 door). Over the last 20 years, different studies showed that tufting and other TTR methods could significantly improve transverse properties and impact resistance, often at the expense of degrading some in-plane properties depending on the tufting parameters used [1-5]. In recent years, modelling work towards understanding the behavior of tufts and their role in TTR composites has been reported [6]. Interlaminar fracture (mostly Mode I) was the most extensively studied with different numerical modelling approaches and bridging laws tested against experimental results. Nevertheless, capturing the different failure mechanisms involved in interlaminar fracture still remains a challenge

at this stage of research since complete studies concentrating on crack bridging behaviour of tufted composites are not available in the literature.

This paper presents the results of a study aiming at better understanding the effects of tuft geometry and tufting patterns with respect to interlaminar fracture. To investigate the effect of tuft geometry, standard tufted Mode I DCB specimens (with top and bottom surface loops) are tested and compared against specimens with surface loops removed. To isolate the contribution of tufts to interlaminar fracture, tufted specimens are tested and compared with tufted specimens that have a full-length film at laminate mid-plane, and non-tufted specimens. Three different tufting patterns are also tested to investigate the effect of tufting density and pattern on interlaminar fracture. Finally, a FE-model, using cohesive elements to represent the delamination at crack plane and connector elements to represent the contribution of discrete tufts, is built and compared against experimental results.

### 3 MATERIALS AND METHODS

#### 3.1 Methodology and test plan

The methodology and test plan (see Table 1) follow a systematic approach and are all based on mode I testing standards (ASTM D5528-01, 2007) [7]. As a first step, on a 5mm square tufting pattern (4 tufts/cm<sup>2</sup>), DCB specimens that included a full-length film at laminate mid-plane are tested and compared against normal tufted specimens and a reference non-tufted specimen. This allows for the exact contribution of tufts to fracture resistance to be determined. This study was performed on the standard (with loops) and the loop-less (loops milled-down) tuft geometry. To evaluate the effect of tufting patterns and density with respect to fracture resistance, two extra tufting patterns are then tested: a 4mm square pattern (6 tufts/cm<sup>2</sup>) and a 5mm staggered pattern (7.2 tufts/cm<sup>2</sup>). Again, both tuft geometry types earlier discussed are tested for these tufting patterns.

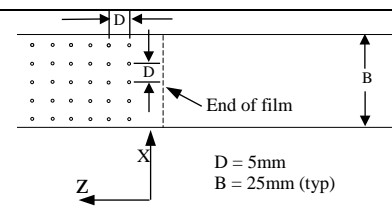
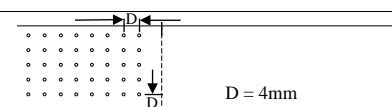
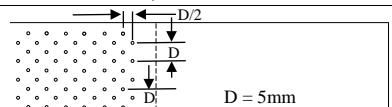
Series/pattern		Nomenclature		Nb. of samples
Type	Pattern/density	Name	Description	
Non-tufted	-	nT, nT-PMMA	Non-tufted reference DCB specimen	3+2
5mm square 4 tufts/cm <sup>2</sup>	 <p>D = 5mm B = 25mm (typ)</p>	5_SQ	5mm square pattern (standard tufts)	3
		5_SQM	5_SQ with surface loops milled-down	3
		5F_SQ	5_SQ with film inserted at mid-plane	3
		5F_SQM	5_SQM with film inserted at mid-plane	3
4mm square 6 tufts/cm <sup>2</sup>	 <p>D = 4mm</p>	4_SQ	4mm square pattern (standard tufts)	3
		4_SQM	4_SQ with surface loops milled-down	3
5mm staggered 7.2 tufts/cm <sup>2</sup>	 <p>D = 5mm</p>	5_ST	5mm staggered pattern (standard tufts)	3
		5_STM	5_ST with surface loops milled-down	3

Table 1. DCB specimen description and nomenclature

In a parallel study, for modelling purposes, tuft pull tests on both tuft geometries are performed to determine the force/displacement relationship to be used in the numerical model (see section 3.5). Non-tufted tensile specimens

## INTERLAMINAR FRACTURE IN TUFTED COMPOSITES: EFFECTS OF TUFT GEOMETRY AND SURFACE DENSITY

and 10x9 cm<sup>2</sup> plate-specimens for all types of laminates are also manufactured to determine the necessary FE-element input mechanical properties. The 9x10 cm<sup>2</sup> specimens are used to perform a modal analysis identification procedure [8] and the non-tufted specimens are used for simple tensile experiments according to [9].

### 3.2 Materials and specimen preparation

Groupe CTT, a textile research center in Québec, Canada, produced five 40x60 cm<sup>2</sup> flat preforms using a KSL (Keilmann Sondermaschinenbau GmbH) RS 522 tufting head. Preforms are made with 30 layers of twill 2/2 glass fabric from Texonic (TG-09-T (305 g/m<sup>2</sup>)) tufted with a 2x 1k-67TEX Tenax HTA-40 carbon fiber thread from Schappe Technique. On these five preforms, specimens are randomly distributed and sufficiently spaced to get a similar amount of tufting on each plate and limit bundle drag-out due to tufting (see Figure 1a and 1b) [10]. After shaving the tufting loops down to 2-3 mm (see Figure 1c), the preforms are vacuum infused on a flat plate using Huntsman's Araldite® LY 8615/Aradur® 8615 epoxy resin system to produce the composite laminates. A caul plate is placed above the preform during infusion to ensure a similar fiber volume content for each specimen and eliminate the typical laminate thickness increase above tufted areas when only a flexible membrane is used above the preform (see Figure 1d) [10]. Cure is performed at 40°C for 24 hours followed by a 3 hour post-cure at 180°C. All specimens are then cut to desired dimensions using a diamond saw. Specimens dedicated to the loop-less series are surfaced machined (-1.5mm) on a CNC milling machine. To complete the preparation, tufted DCB specimens are reinforced with polymethyl-methacrylate (PMMA) beams to prevent specimen failure in bending and allow observation of the crack front from above during testing. To do so, the PMMA surface is prepared by sandblasting and then glued with Loctite® 454 cyanoacrylate adhesive (gel form).

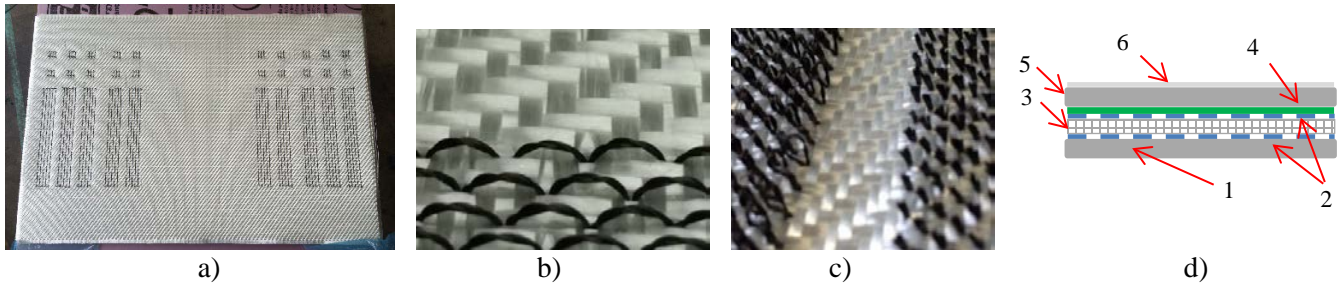


Figure 1. Preform manufacturing and infusion set-up: a) 40x60 cm<sup>2</sup> preform prior to infusion, b) Top view of tufted area, c) Bottom view of tufted area with loops intact (left) and shaved (right), d) Vacuum infusion set-up (1- Molding plate, 2- peel ply, 3- preform, 4- flow mesh, 5- caul plate, 6- vacuum bag).

### 3.3 Mechanical properties for modelling purposes

Mechanical and physical properties used for modeling purposes are summarized in Table 2. Longitudinal tensile properties of the non-tufted composite are determined according to the normalized testing procedure proposed in ASTM D3039 [9]. Glass volume content ( $V_{f-Gf}$ ) and tuft volume content ( $V_{f-Cf}$ ) for all laminates are measured according to the testing procedure proposed in ASTM D3171 [11] using the matrix burn-off method (procedure G). Most of the remaining mechanical properties are found from modal analysis identification with the 9x10 cm<sup>2</sup> specimens mentioned in sections 3.1 under excitation frequencies up to 10 kHz while the remaining properties are found in literature [12]. For details about the modal analysis identification procedure, the reader is referred to the work of Cugnoni et al. [8].

### 3.4 Fracture testing and R-Curves assessment

The experiments carried out to characterize interlaminar fracture follow the procedure proposed in ASTM Standard D5528-01 [7] and use standard Mode I DCB specimens and test rig. Tests are performed at room temperature on a Shimadzu® AGS electromechanical testing machine equipped with a 5 kN load-cell (see Figure 2). The specimens (pre-cracked with a 65mm long, 13 $\mu$ m thick ETFE film) are loaded at a displacement rate of 2 mm/min and monitored with two synchronized high-resolution CCD cameras (side and top view). All R-curves presented in this work are prepared with the modified compliance calibration method [7] using the load, displacement and crack advance data.

Name	$E_z$ (GPa)	$E_x$ (GPa)	$E_y$ (GPa)	$G_{zx}$ (GPa)	$G_{xy}=G_{zy}$ (GPa)	$\nu_{zx}$	$\nu_{zy}$	$\nu_{xy}$	$V_{f-Gf}$ [%]	$V_{f-Cf}$ [%]
Non-tufted	<b>24.9</b>	11.6	<b>24.9</b>	<u>5.5</u>	<u>6.4</u>	<b>0.12</b>	0.15	0.2	<b>52.45</b>	-
<b>5-SQ</b>	<u>29.8</u>	“	<u>26.5</u>	<u>5.7</u>	<u>5.7</u>	“	“	“	<b>48.81</b>	<b>0.49</b>
<b>4-SQ</b>	<u>28.7</u>	“	<u>26.7</u>	<u>5.5</u>	<u>5</u>	“	“	“	<b>47.44</b>	<b>0.44</b>
<b>5-ST</b>	<u>24.9</u>	“	<u>27</u>	<u>5.5</u>	<u>4.6</u>	“	“	“	<b>46.19</b>	<b>0.65</b>
<b>5-SQM</b>	<u>29.4</u>	“	<u>26.5</u>	<u>5.5</u>	<u>5.7</u>	“	“	“	<b>51.32</b>	<b>0.29</b>
<b>4-SQM</b>	<u>28.7</u>	“	<u>26.2</u>	<u>5.5</u>	<u>5</u>	“	“	“	<b>48.91</b>	<b>0.34</b>
<b>5-STM</b>	<u>24.7</u>	“	<u>27</u>	<u>5.1</u>	<u>4.5</u>	“	“	“	<b>47.77</b>	<b>0.34</b>

Table 2. Material properties and engineering constants of the DCB specimens (Bold: experimental, Underline: modal analysis, Rest: literature).

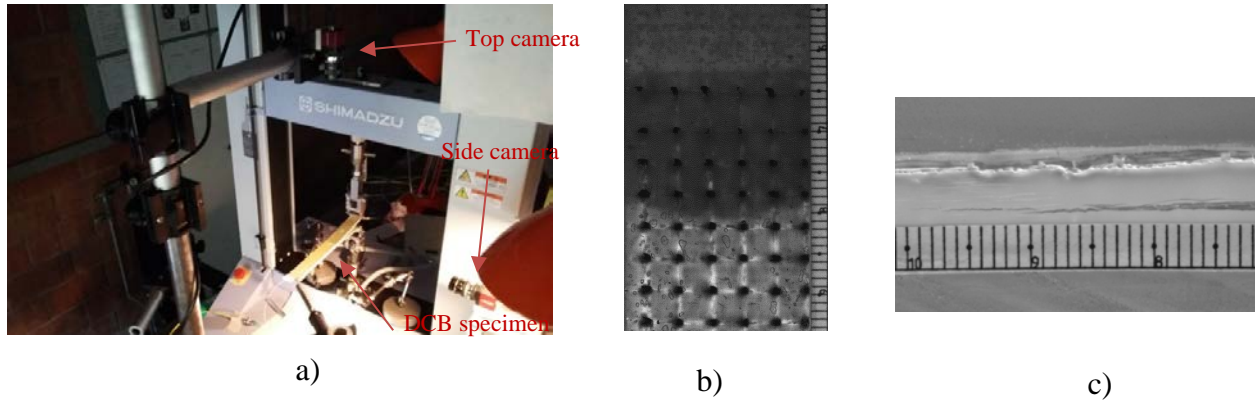


Figure 2. Mode 1 testing apparatus: a) General view of the set-up, b) top view (4-SQM pattern), c) side view.

### 3.5 Numerical methods

The identification of the traction-separation relation corresponding to the tow/ply bridging phenomena present during crack propagation follows the procedure described in [13-14] and references therein. This identification procedure is based on strain measurements acquired from an optical fiber bonded on the upper surface of a regular, non-PMMA reinforced, non-tufted DCB specimen, with 10 multiplexed fiber Bragg gratings (FBG) inscribed in a single mode, simple optical fiber with an external diameter of 125 $\mu$ m. The grating length is 1mm and the reflected Bragg wavelengths are equally spaced between 1520 and 1565 nm. A numerical model of the DCB experiment is built with a variable bridging traction profile,  $\sigma_b(z)$ , (Figure 3a) and the corresponding numerical strains are compared with the strain data recorded by the FBGs. An iterative procedure minimizes the error between the experimental and simulated strains, as well as the difference between the simulated J-integral and the

## INTERLAMINAR FRACTURE IN TUFTED COMPOSITES: EFFECTS OF TUFT GEOMETRY AND SURFACE DENSITY

experimentally evaluated initial fracture toughness,  $G_{l,i}$ , as described in [13-14]. The result of this procedure is a traction-separation relation,  $\hat{\sigma}(\delta)$  (see Figure 3b), that is used for the calculation of the ERR and prediction of the load history using cohesive element modeling.

The described technique is applied on a non-tufted, non-PMMA reinforced specimen to increase the sensitivity of the FBGs to the closing tractions due to bridging. The closing traction profile is calculated for the aforementioned specimen and is extrapolated for the PMMA reinforced case using a scaling relationship based on the stiffening of the arms and the findings of [13] and references therein, to evaluate the traction profile exponent,  $\gamma$ .

Consequently, 2D plain strain FE models of the DCB specimens are created in Abaqus Standard v6.12, to predict the load-displacement response, comprising a zone of cohesive elements (Abaqus COH2D4) with identified traction-separation relation to model the bridging phenomena on the delamination plane. Moreover, connector line-elements (Abaqus CONN2D2) are superimposed to the cohesive zone, with each connector to represent one row of tufts, based on the acquired response from the tuft pull tests, normalized per single tuft. In all created numerical models, the boundary conditions shown in Figure 3a, are applied.

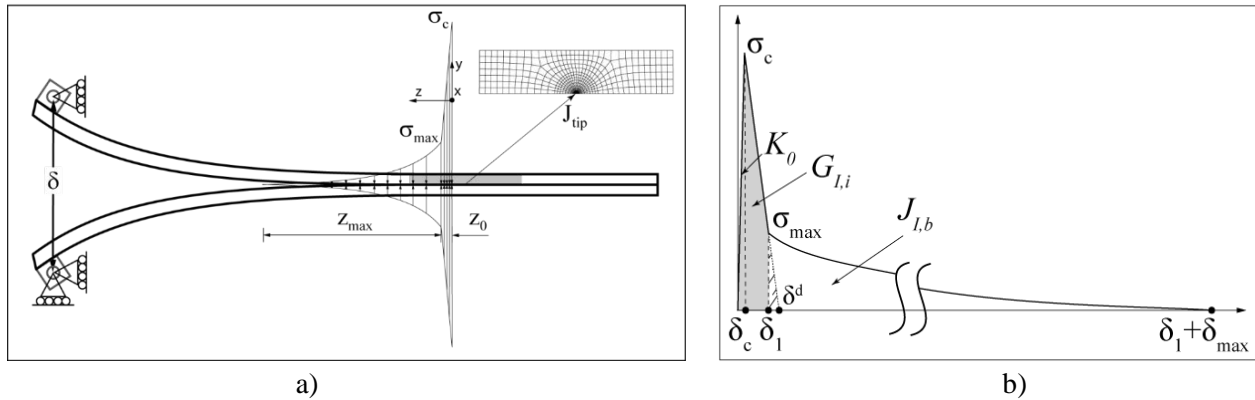


Figure 3. Delamination modeling: a) Numerical model used for the identification scheme b) Schematic of the traction-separation relation used in the cohesive zone modeling.

## 4 EXPERIMENTAL RESULTS

### 4.1 Contributions of tufts and ply delamination to fracture resistance

To serve as a baseline for comparison, non-tufted specimens cut from the plates described in section 3.2 are reinforced with PMMA beams and tested (see Figures 4a and 5a). For these specimens, an ERR at steady state of approximately  $0.9\text{kJ/m}^2$  is obtained. The fractured surface shows that some interaction between the upper and lower plies occur at the crack plane. During the test, moderate ply or tow bridging is observed (see Figure 2c) leading to the R-curve behavior of the non-tufted material (see Figure 4a). For completeness, the data of the non-PMMA reinforced specimens and the FBG equipped specimen (mentioned in section 3.5) are also illustrated on Figure 4a and 5a.

Using the 5mm square tufting pattern, specimens of both tuft geometry are tested. A first series with a full-length release film at laminate mid-plane is tested to quantify the contribution of tufts alone to fracture resistance. The tufted specimens with loops (5F\_SQ) (Figure 4b) have an ERR at steady state of around  $2\text{kJ/m}^2$  while tufted specimens with loops milled-down (5F\_SQM) (Figure 5b) reached around  $3.5\text{kJ/m}^2$ . This increase in fracture resistance is attributed to the significant difference in failure mechanism between the two tuft geometries, the former having tufts breaking flat at laminate mid-plane, while for the later, tufts pulling-out of the laminate.



Results for conventional tufted DCB specimens (5\_SQ and 5\_SQM) are shown in Figures 4c and 5c. Specimens with loops (Figure 4c) yield an average ERR at steady state of approximately  $3\text{kJ/m}^2$ , which is almost equal to the sum of maximum measured ERRs of the non-tufted (Figure 4a) and the 5F\_SQ series (Figure 4b), suggesting that tufts do not significantly affect the inter-ply fracture mechanism occurring in non-tufted composites. This can be correlated to the fact that the fractured surface of figure 4c is very similar to figure 4a. As seen on Figure 5c, specimens without tufting loops show a somewhat similar behavior suggesting that the same superposition principle can be applied for this tuft geometry. In this case, the sum of steady state ERR of Figures 5a and 5b is approximately 10% less than the steady state ERR in Figure 5c. This could be attributed to the change in fracture mechanism of the laminate around the tufts that are pulling out since it was observed during testing that ply/tow bridging during crack advance was more pronounced for loop-less tufted specimens.

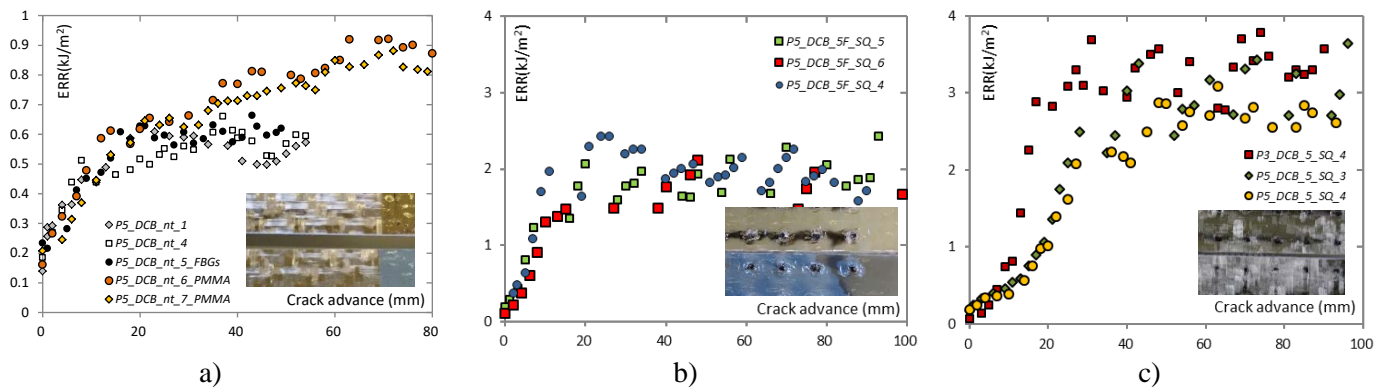


Figure 4. Experimental R-curves and fractured surfaces for the standard tufting geometry (with loops) and reference non-tufted (nT) specimens: a) nT specimens, b) 5F\_SQ specimens (with film at crack-plane), c) 5\_SQ specimens.

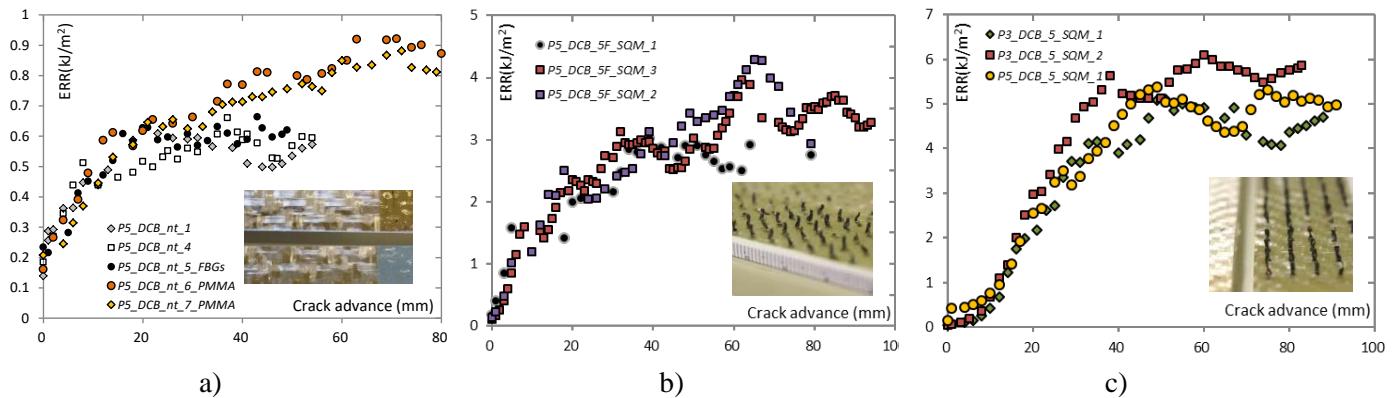


Figure 5. Experimental R-curves and fractured surfaces for the loop-less tufting geometry (with loops milled-down) and reference non-tufted (nT) specimens: a) nT specimens, b) 5F\_SQM specimens (with film at crack-plane), c) 5\_SQM specimens.

#### 4.2 Effect of tufting areal density and pattern type

Two new tufting patterns are tested to investigate the effect of tufting areal density and pattern type on fracture resistance. A 4mm square pattern ( $6\text{ tufts/cm}^2$ ) and a 5mm staggered pattern ( $7.2\text{ tufts/cm}^2$ ) are compared to the

## INTERLAMINAR FRACTURE IN TUFTED COMPOSITES: EFFECTS OF TUFT GEOMETRY AND SURFACE DENSITY

results of the 5mm square pattern (4 tufts/cm<sup>2</sup>) presented in section 4.1. Results on Figure 6a and 6b show that fracture resistance can be significantly improved with these new patterns and can almost be increased by a full order of magnitude when compared to the non-tufted composites. When applying the superposition principle discussed in section 4.1 to these new patterns, it can be concluded that ERR at steady state does not directly scale to tuft areal density (red lines in Figure 6a and 6b). This suggests that tuft resistance and/or laminate fracture resistance is influenced by tuft density and pattern, and in the case of the patterns studied here, superposing the contribution of tufts scaled and laminate fracture resistance, underestimates ERR at steady state by 25-30% for both tufting geometry.

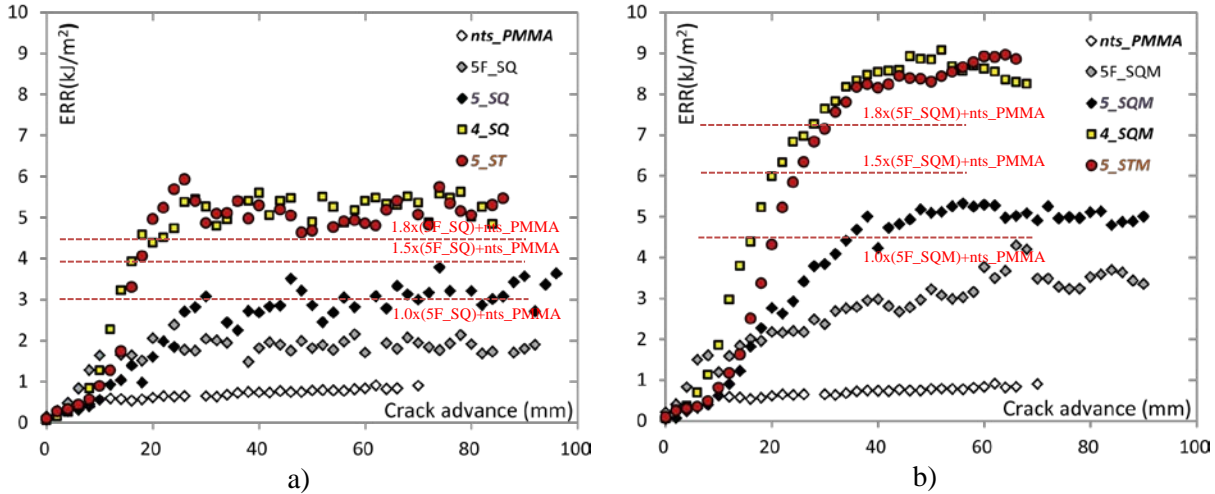


Figure 6: Average experimental R-curves showing the effect of tufting patterns on fracture resistance: a) Standard tufting series, b) Series with tufting loops milled down. (Note: nts\_PMMA is a non-tufted reference specimen and 5F\_SQ and 5F\_SQM specimens are specimens in which only tufts contribute to fracture resistance, see Table 1)

## 5 NUMERICAL MODELING

### 5.1 Traction separation

#### 5.1.1 Identification of non-tufted composite bridging traction

The identified traction-separation relations for the non-tufted DCB specimens (regular (nT) and PMMA reinforced (nT\_PMMA)) are illustrated in Figure 7a. These identified and estimated traction separation relations are used in the cohesive element model to predict the load-displacement response.

The acquired numerical response is compared with the experimental results in Figure 7b and both the regular and PMMA reinforced GFRP are in good agreement. As a result, it is considered that the identified traction-separation relations describe well the tow/ply bridging phenomena for the non-tufted specimens.

#### 5.1.2 Identification of tufts force-separation relations

To obtain the force-separation response of the regular tufts and loop-less ones, tuft pull-tests are performed. The test coupons have a surface of 20 x 20 mm<sup>2</sup>, comprise 9 tufts of the 5mm square pattern and have a release film introduced at laminate mid-plane during the fabrication of the preform. Thus, the contribution of bridging tufts is isolated from the delamination response of the composite. A photograph of the specimen during testing is shown in Figure 8a.

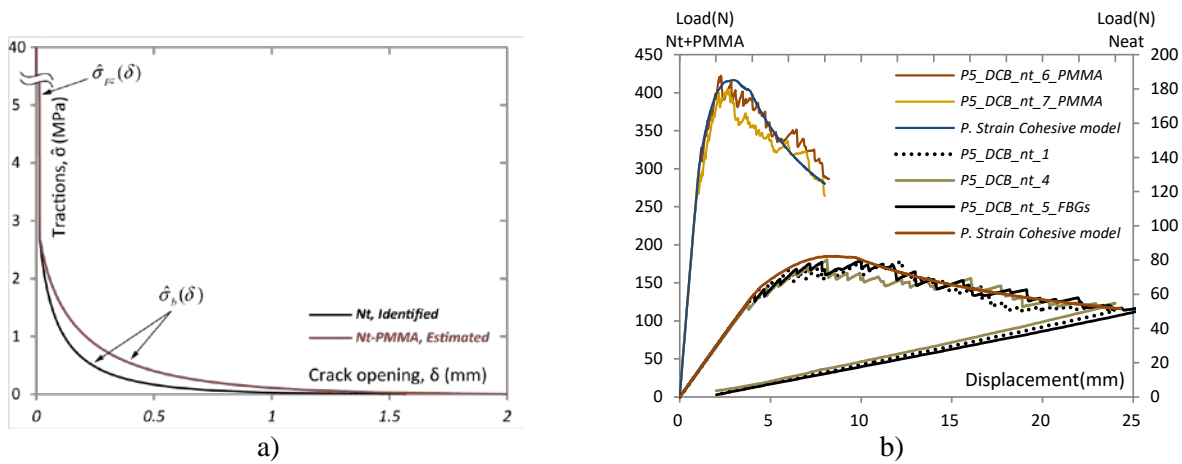


Figure 7. Cohesive law and FE modeling of non-tufted specimens: a) Bridging traction profiles b) Experimental and numerical load-displacement results.

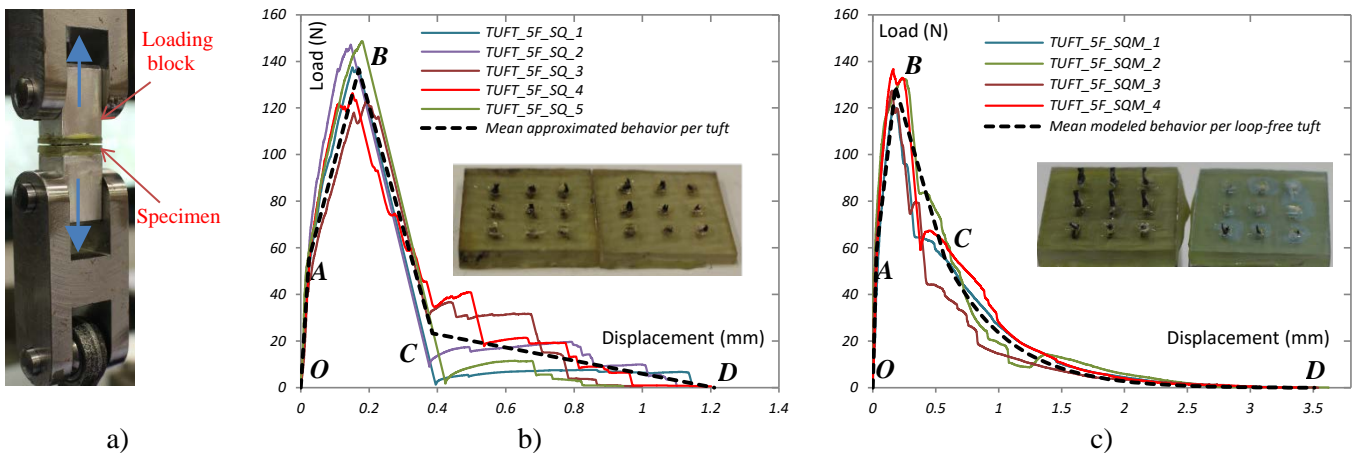


Figure 8. Pull-test on 20 x 20 mm<sup>2</sup> tufted samples (9 tufts (5mm square pattern)): a) test jig, b) load-displacement results and fractured surface for standard tufting specimens (with loops), c) load-displacement results and fractured surface for loop-less (milled-down) specimens. Note: load is normalized for one tuft.

The load-displacement responses of the two series, standard and loop-less tufts (normalized per tuft), are depicted in Figure 8b and 8c respectively. In these graphs, four key points can be located. (A) is the end of linear response of the tuft. After this point, a quasi-linear hardening is shown up to point (B) which corresponds to the ultimate strength of the tuft. After point (B), a sudden drop to point (C) is depicted where major failure is observed. This point corresponds to significant damage of the tuft threads in the mid-plane for the standard tufts, while for the loop-less tufts, it corresponds to debonding of the tuft from the host material. For the standard tufts, the last part corresponds to the breaking of the residual intact matrix and fibers, until the ultimate failure of the tuft at point (D) is reached. On the other hand, the last part for the loop-less ones corresponds to the pull-out of the tuft from the host material, dominated by the friction forces on the interfaces. The total absorbed energy per tuft for the standard tufts is measured as 41.2 mJ  $\pm$  7.3% and for the loop-less tufts as 78 mJ  $\pm$  12.5%. Figure 8b also shows the mean



## INTERLAMINAR FRACTURE IN TUFTED COMPOSITES: EFFECTS OF TUFT GEOMETRY AND SURFACE DENSITY

approximated behaviors per regular tuft as implemented in the connector elements, comprising four linear segments. The corresponding mean response for the loop-less tufts is also included in Figure 8c, where three linear segments are used followed by an exponential softening response.

### 5.1.3 DCB experiment modeling

The predicted load-displacement response for the 5\_SQ and 5\_SQM series are shown in Figure 9a and 9b respectively, while the insert in 9a depicts the created numerical model including the cohesive element zone to model the delamination and tow/ply bridging phenomena and the connector elements to model tuft bridging. The data in these Figures show that the numerical analog of the DCB experiments predicts well the actual experiment until the maximum load, with an underestimation of ~10% for the following part, for the standard tuft series. A similar behavior is depicted for the loop-less DCBs with some higher underestimation, indicating interactions of the delamination and tuft bridging phenomena, analogous to the superposition of the ERRs (see Section 4.1)

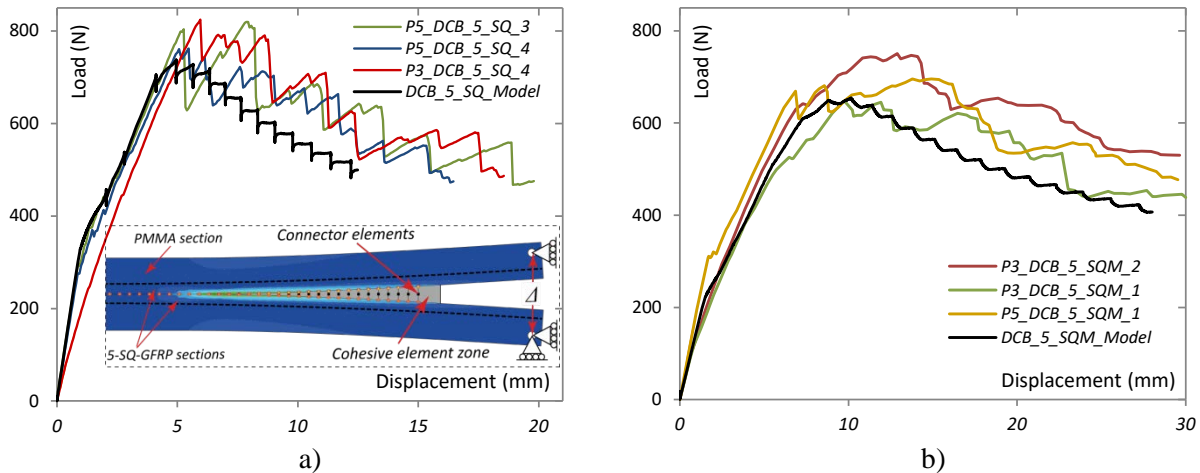


Figure 9. DCB simulations vs. experimental data for the 5mm square tufted specimens: a) Standard tufting specimens (with loops) and snapshot from the FE model as insert, b) Loop-less (milled-down) tufting specimens.

## 6 CONCLUSIONS

We proposed a systematic approach based on Mode I testing to firstly quantify the exact contribution of tufts in the delamination process of tufted composite, and second, evaluate the influence of tufting pattern and density on fracture resistance. In both cases, two tuft geometries were evaluated. A standard tuft geometry with loops present on top and bottom of the laminate and a loop-less geometry, with top and bottom loops milled-down.

To quantify the contribution of tufts in the delamination process, using a 5mm square tufting pattern (4 tufts/cm<sup>2</sup>), tufted DCB specimens that included a full-length film at laminate mid-plane were tested and compared against normal tufted specimens and reference non-tufted specimens. For this tufting pattern, experimental and simulated results demonstrated that interactions between the tuft failure mechanism and the ply/tow bridging phenomena seem to be small since the contribution of ply delamination and tuft resistance can be superposed to predict fracture resistance of tufted composites within 10% error.

To evaluate the effect of tufting patterns and density with respect to fracture resistance, two extra tufting patterns were tested: a 4mm square pattern (6 tufts/cm<sup>2</sup>) and a 5mm staggered pattern (7.2 tufts/cm<sup>2</sup>). Again, both tuft

geometries discussed earlier were tested for this series of tests. For these new patterns, it was demonstrated that simply up-scaling the tuft resistance based on the previously tested 5mm square pattern and superposing it to the contribution of ply delamination based on non-tufted specimens, would not serve as a good approximation of the tufted specimens. These results showed that the interaction between the tuft failure mechanism and the ply/tow bridging phenomena can eventually become significant depending on the tufting density and type of tufting pattern used.

## 7 ACKNOWLEDGEMENT

The authors would like to acknowledge Groupe CTT, Saint-Hyacinthe, Québec, Canada, for the production of the tufted preforms and Dr. Joël Cugnoni for his help to identify the mechanical properties of the composites.

## 8 REFERENCES

- [1] A.P. Mouritz, K.H. Leong, and I. Herszberg. A review of the effect of stitching on the in-plane mechanical properties of fibre-reinforced polymer composites. *Composites Part A: Applied Science and Manufacturing*, 28(12):979 – 991, 1997.
- [2] C. Scarponi, A.M. Perillo, L. Cutillo, C. Foglio, Advanced TTT composite materials for aeronautical purposes : Compression after impact (CAI) behaviour, *Composite: Part B* (2006), vol 38, 258-264.
- [3] J. W. G. Treiber, Performance of tufted carbon fibre/epoxy Composites, PhD Thesis, Cranfield University, 2011.
- [4] C., Leduc, S., Joncas, J-S, Leclerc. «Effects of one-side stitching parameters on damage tolerance of carbon-poxy laminates.», 16th European Conference on Composite Materials, Séville, Espagne, June 22-26, 2014.
- [5] S., Morin, S., Joncas. «Structural properties of stitched T-stiffeners: web tear-off and column buckling.», 10th International Conference on Composite Science and Technology ICCST/10, Lisbon, Portugal, September 2-4, 2015.
- [6] C. Osmiani, G. Mohamed, J. Treiber, G. Allegri and I. Partridge, "Exploring the influence of micro-structure on the mechanical properties and crack bridging mechanisms of fibrous tufts," *Composites Part A: Applied Science and Manufacturing*, vol. 91, no. Part 2, pp. 409-419, 2016.
- [7] ASTM Standard D5528–01, Standard Test Method for Mode I Interlaminar Fracture Toughness of Unidirectional Fiber-Reinforced Polymer Matrix Composites, West Conshohocken, PA: ASTM International, 2007.
- [8] J. Cugnoni, T. Gmur and A. Schorderet, "Inverse method based on modal analysis for characterizing the constitutive properties of thick composite plates," *Computers and Structures*, vol. 85, no. 17, pp. 1310-1320, 2007.
- [9] ASTM Standard D3039/D3039M–14, Standard Test Method for Tensile Properties of Polymer Matrix Composite Materials, West Conshohocken, PA: ASTM International, 2014.
- [10] G. Dell'Anno, J.W.G. Treiber, I.K. Partridge, Manufacturing of Composite Parts Reinforced Through-Thickness by Tufting, *Robotics and Computer-Integrated Manufacturing*, Vol. 37, (2017), 262-272.
- [11] ASTM Standard D3171–15, Standard Test Methods for Constituent Content of Composite Materials, West Conshohocken, PA: ASTM International, 2015.
- [12] I. Daniel and O. Ishai, *Engineering Mechanics of Composite Materials*, New York: Oxford University Press, 1994.
- [13] G. Pappas and J. Botsis, "Intralaminar fracture of unidirectional carbon/epoxy composite: experimental results and numerical analysis," *International Journal of Solids and Structures*, Vols. 85-86, pp. 114-124, 2016.
- [14] G. Pappas, L. Canal and J. Botsis, "Characterization of intralaminar mode I fracture of AS4/PPS composite using inverse identification and micromechanics," *Composites: Part A*, vol. 91, pp. 117-126, 2016.